Pulsed-laser crystallization of amorphous silicon layers buried in a crystalline matrix

A. Polman,[a] P. A. Stolk, D. J. W. Mous, and W. C. Sinke
FOM-Institute for Atomic and Molecular Physics, Kruislaan 407, 1098 SJ Amsterdam, The Netherlands
C. W. T. Bulle-Lieuwma and D. E. W. Vandenhoudt
Philips Research Laboratories, P. O. Box 80 000, 5600 JA Eindhoven, The Netherlands

(Received 31 July 1989; accepted for publication 3 January 1990)

Ion implantation, employing Si, Ar, and Cu ions in the energy range from 275 to 600 keV, was used to form amorphous silicon layers buried in a crystalline matrix. Different layer geometries were produced, with 150–620-nm-thick amorphous layers, separated from the surface by 120–350-nm-thick crystalline layers. Crystallization of the amorphous layers was induced by 32-ns pulsed ruby laser irradiation. Real-time reflectivity and conductivity measurements indicate that internal melting can be initiated at the amorphous-crystalline interface, immediately followed by explosive crystallization of the buried layer. Channeling and cross-section transmission electron microscopy reveal that in both Si(100) and Si(111) samples explosive crystallization proceeds epitaxially with twin formation, the twin density being higher in Si(111) than in Si(100). The measured crystal growth velocities range from 15 to 16 m/s, close to the fundamental limit for crystalline ordering at a Si liquid-crystalline interface. Computer modeling of heat flow and phase transformations supports the experimental data.

I. INTRODUCTION

Ion implantation is at present a well-established technique for the controlled introduction of dopants into semiconductors. Due to extensive research during the past two decades, by now detailed knowledge is available of the ion-solid interactions for medium energy (20–200 keV) ions.[1,2] Recently, this area of research is being extended to higher energies, up to ≈ 1 MeV, for which the ion range can be several micrometers. For high-energy irradiation the nuclear and electronic stopping processes exhibit a wide range over the ion trajectory, leading to different damage formation mechanisms as a function of depth in the sample. In this case, amorphization is usually initiated deep in the sample where the defect formation rate is maximal.

In the present experiments, Si(100) and Si(111) samples were implanted with $^{28}Si^+$, $^{40}Ar^+$ or $^{63}Cu^+$ ions in the energy range from 275 to 600 keV. Amorphous (a-Si) layers with a thickness ranging from 150 to 620 nm were formed, buried under crystalline (c-Si) surface layers of 130–350 nm in thickness.

The purpose of this work is to investigate the use of pulsed-laser irradiation to crystallize buried amorphous layers. During the last 10 years, pulsed-laser irradiation has been employed as a method to anneal implantation-induced lattice damage in silicon.[3,4] Using high-energy-density laser pulses, it has been shown that recrystallization of amorphous surface layers can be achieved via melting of the complete a-Si layer, followed by epitaxial solidification from the c-Si substrate. For low-energy irradiation of amorphous surface layers, "explosive" crystallization (EC) can occur. This effect has been observed by several workers during the last few years.[5–13] Under specific conditions of irradiation and sample structure, a shallow region of a-Si at the surface is heated and melted, whereupon a self-propagating ("explosive") melting and solidification process, driven by the difference in latent heat of melting for amorphous and crystalline Si, transforms the amorphous layer to crystalline Si. EC of amorphous surface layers yields randomly oriented, fine-grain (≈ 100 Å) polycrystalline Si.[5,7,8,10,13] This microstructure originates from the specific nucleation events which sustain EC. The precise nature of the processes that trigger and sustain EC is still under debate.[10,14–16]

In the present experiments, pulsed-laser irradiation was employed for the first time to crystallize amorphous Si layers buried in a crystalline matrix.[17] The experiments show that, using a 32-ns laser pulse, melting can be initiated in a very shallow region of the buried amorphous layer. Hereafter, an *epitaxial explosive crystallization* process, driven by the difference in latent heat between a-Si and c-Si, is initiated. This self-sustained process converts the buried amorphous layer to single-crystalline Si, epitaxially aligned with the crystalline surface. The kinetics of these rapid phase transformations are studied in detail using time-resolved techniques. The microstructure before and after irradiation is investigated.

II. EXPERIMENT

A. Ion implantation

Single crystals of Si with either (100)- or (111)-oriented polished surfaces, as well as 500-nm silicon-on-sapphire (SOS) samples, were implanted at room temperature at a base pressure below 10^{-6} mbar. For implantation in a random direction, wafers were tilted 7° from a plane perpendicular to the ion beam, with the tilt axis rotated 20° from a [011] wafer flat. Cu implantations were performed in a (011) planar channeling geometry; in this case the sample

[a] Present address: AT&T Bell Laboratories, 600 Mountain Avenue, Murray Hill, NJ 07974.

 0021-8979/90/094024-12$03.00

was also tilted 7°, but with the tilt axis parallel to the flat. During both the random and the channeling implantations, the ion beam was scanned electrostatically over the sample. The peak current density in the ≈10-mm-diam beam spot, measured on a 10-mm^2 Faraday cup, was typically 3–4 μA/cm^2, whereas scanning of the beam resulted in a current density of 300–400 nA/cm^2 on target. During Si^+ implantation, samples were mounted on the polished surface of a sample holder containing a thermocouple. The maximum recorded temperature rise of the holder during implantation amounted to 55 °C. In addition, a pyrometer with a lower-limit temperature sensitivity of ≈150 °C was used to monitor the sample infrared emissivity. Never during implantation was a noticeable signal detected. Part of the implanted samples was annealed in a standard tube furnace either under flowing N_2 or in vacuum at a base pressure below 10^{-6} mbar.

B. Pulsed-laser irradiation and transient techniques

Pulsed-laser irradiation was performed using a *Q*-switched ruby laser [wavelength $\lambda = 694$ nm, pulse duration 32 ns full width at half-maximum (FWHM)]. Using a diaphragm and a lens, a small spatial fraction of the laser beam was projected on the sample under far-field conditions. The lateral homogeneity of the ruby laser spot was determined to be ± 10%. A new location on the implanted sample was used for each laser shot. The laser energy density was varied between 0.1 and 2.0 J/cm^2, and was calibrated using calorimetry. During irradiation, the transient optical reflectivity[18] of the sample was monitored using a continuous-wave AlGaAs laser operating at $\lambda = 825$ nm, incident at 20° to the surface normal and focused to ≈50 μm FWHM. The laser beam was linearly polarized with the polarization plane at an angle of 35° relative to the scattering plane. The reflected intensity was monitored through a narrow-band transmission filter using a Si *p-i-n* photodiode and a fast oscilloscope. The total system rise time was ≈1 ns. The time-resolved reflectivity (TRR) technique probes changes in refractive index and, hence, in combination with proper modeling, enables one to follow phase transformations in real time. Analysis of reflectivity measurements was done using Fresnel matrix calculations for the reflectivity of an isotropic planar multilayer system.[19]

SOS samples were patterned photolithographically to yield samples for transient conductivity measurements.[20] The transient conductance technique, utilizing the 30-fold increase in conductivity of Si upon transformation to the liquid (*l*-Si) phase, monitors the molten Si thickness in real time. Reflectivity and conductivity measurements on SOS samples were performed simultaneously during one single laser shot.

Computer modeling of transient heat flow and phase transformations was performed using a numerical one-dimensional heat-flow code developed by Wood and Geist.[21]

C. Structural analysis

Microstructural analyses were performed using Rutherford backscattering spectrometry (RBS)[22,23] employing a 2-MeV He^+ beam and a scattering angle between 120° and 170°, depending on analysis purpose. Channeling measurements were done with the ion beam aligned with the [100] or [111] direction for Si(100) and Si(111) samples, respectively. In addition, transmission electron microscopy (TEM) was performed. Specimens were prepared in cross-section configuration, the material being thinned to electron transparency by mechanical polishing followed by Ar^+-ion bombardment at 4 keV at grazing incidence.[24] TEM observations were made using a conventional electron microscope operated at 120 keV. The structures in some specimens were examined on an atomic scale using a high-resolution 300-keV microscope with a point resolution of 1.9 Å.

III. BURIED LAYER FORMATION

A. Channeling 450-keV $^{63}Cu^+$ implantation into Si(100)

Channeling implantation conditions are especially suitable for the formation of buried disordered layers in a crystalline matrix. For ion beams aligned with a principal crystal axis or plane, the density of nuclear interactions is reduced with respect to that for randomly oriented beams. This effect is most pronounced near the surface.[25] Si(100) samples were implanted with 450-keV $^{63}Cu^+$ ions to a total dose of 1.5×10^{15} cm^{-2} using a planar channeling geometry. Figure 1 shows a (011) cross-section TEM micrograph of a sample after implantation. The micrograph shows a buried amorphous layer (thickness 370 nm), separated from the surface by a 130-nm-thick crystalline region. The 100-nm top region of this surface layer contains a low density of dislocations. The interface between surface *c*-Si and buried *a*-Si layer is relatively sharp with some *c*-Si islands embedded in the amorphous matrix. A relatively broad defected region is observed in the *c*-Si substrate. This can be understood from the fact that in the initial stage of channeling implantation the penetration depth of the Cu ions is relatively large, resulting in deep crystal damage. During implantation, however, the

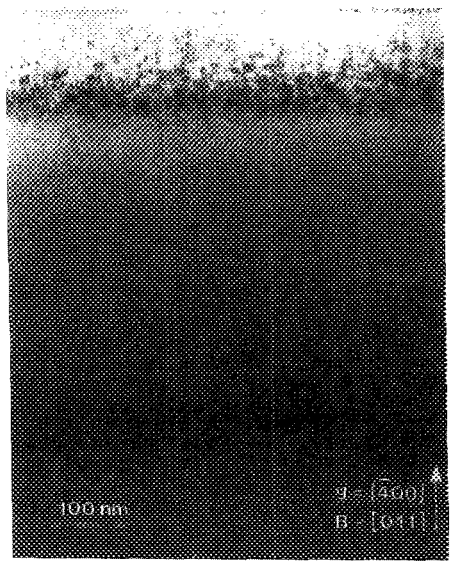

FIG. 1. (011) Cross-section [$\bar{4}$00] bright-field TEM micrograph of a Si(100) sample implanted with 1.5×10^{15} Cu^+ ions/cm^2 at 450 keV in a (011) planar channeling geometry.

FIG. 2. (011) Cross section [$\bar{4}00$] bright-field TEM micrograph of a Si(111) sample implanted with 4.0×10^{15} Si ions/cm^2 at 350 keV and thermally annealed at 490 °C for 15 min.

channeling effect reduces because damage builds up and *a*-Si is formed. Hence the average penetration depth of Cu ions gradually decreases. The overall result is formation of an extended region containing end-of-range (EOR) damage.

B. Random 350-keV $^{28}Si^+$ implantation into Si(100) and Si(111)

Both Si(100) and Si(111) samples were implanted with 350-keV $^{28}Si^+$ ions in a random direction close to the surface normal. The total implantation dose was 4.0×10^{15} ions/cm^2. The calculated projected ion range for this energy is 480 ± 96 nm.[26] By using Si ions in experiments concerning buried layer formation and pulsed-laser crystallization in silicon, any effect which might result from the use of a chemically dissimilar ion can be excluded. Following implantation, the samples were thermally annealed in vacuum at 490 °C for 15 min. Channeling analysis indicates that this thermal treatment reduces the implantation damage in the near-surface region. This damage might consist of simple defects (e.g., divacancies[27]) and small amorphous clusters[28] which can be crystallized by solid-phase epitaxy (SPE).[29] From channeling[30] it is derived that in both the Si(100) and the Si(111) sample implantation followed by thermal annealing leads to formation of 420-nm-thick buried amorphous layers. The thickness of the *c*-Si surface layer amounts to 130 nm in the Si(100) sample and to 120 nm in the Si(111) sample.

The microstructure after thermal annealing was studied in detail using cross-section TEM. Figure 2 shows a (011) cross section of an implanted Si(111) sample after thermal annealing. The micrograph shows a buried amorphous layer (thickness 420 nm), separated from the surface by a 120-nm-thick crystalline region. In the *c*-Si surface layer, small dislocation loops are detected which are probably formed during annealing. The interface between the *a*-Si layer and the *c*-Si surface is undulating over ≈50 nm. This is a result of the random nature of the damage formation process which produces a broad transition region containing amorphous and crystalline areas. During annealing, growth of randomly distributed *c*-Si clusters results in a nonplanar interface region. The micrograph also reveals that the back-side interface between the buried *a*-Si layer and the *c*-Si substrate is sharp within 20 nm. This can be understood from the fact that near the EOR of the implanted ions the damage formation rate decreases rapidly with depth. As a result, this transition region from *a*-Si to *c*-Si is relatively narrow.

C. Other implantations

Additional experiments were performed using buried *a*-Si layers produced by 275-keV $^{40}Ar^+$ implantation into SOS as well as by 600-keV $^{28}Si^+$ implantation into Si(100). Table I summarizes the implantation conditions and the resulting layer structures for these samples as well as for those described in the previous sections.

IV. PULSED-LASER IRRADIATION

A. Cu-implanted samples

1. Time-resolved reflectivity

Cu-implanted Si(100) specimens were irradiated with a ruby laser pulse. Figure 3 shows a compilation of TRR measurements performed during irradiation at several laser energy densities. Below 0.13 J/cm^2, no change in the reflectivity is detected. For energy densities between 0.14 and 0.23 J/cm^2, pronounced oscillations are observed. As has been

TABLE I. Implantation conditions for the samples studied in this work. "r/ch" indicates random or channeling implantation geometry, "*c*-Si" and "*a*-Si" denote layer thickness for surface *c*-Si and buried *a*-Si layers, respectively.

Target	Ion energy (keV)	Dose (10^{15} atoms/cm^2)	r/ch	Annealing time and temperature	*c*-Si (nm)	*a*-Si (nm)
Si(100)	Cu^+ 450	1.5	ch	...	130	370
Si(100)	Si^+ 350	4.0	r	15 min, 490 °C	130	420
Si(111)	Si^+ 350	4.0	r	15 min, 490 °C	120	420
(100)SOS	Ar^+ 275	0.6	r	15 min, 455 °C	140	150
Si(100)	Si^+ 600	15	r	15 min, 490 °C	350	620

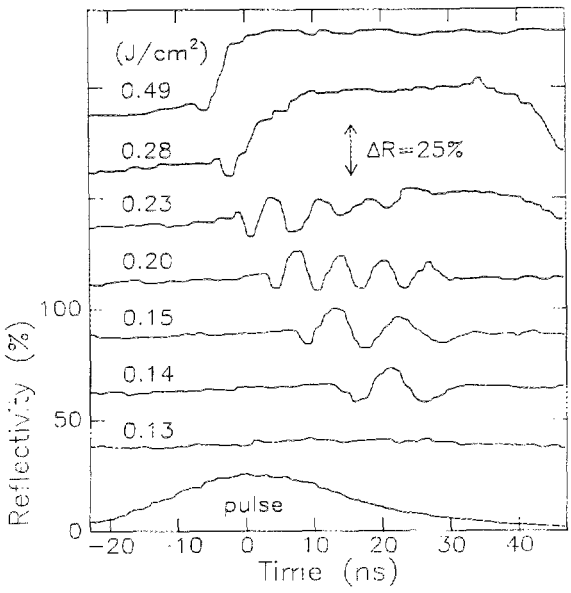

FIG. 3. Transient reflectivity measurements recorded during pulsed-laser irradiation of Cu-implanted samples at different laser energy densities (indicated in the figure). The reflectivity scale corresponding to the transient of 0.13 J/cm^2 is given in the figure. Subsequent transients are each shifted by an absolute value of 25% for clarity. The laser pulse profile is shown at the bottom.

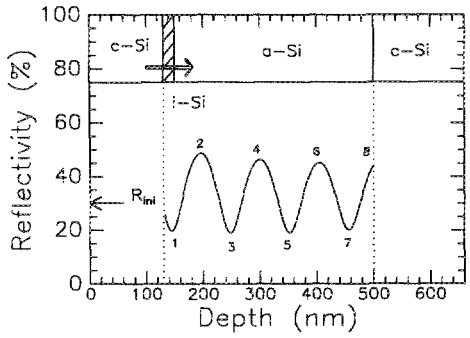

FIG. 4. Calculated optical reflectivity of a c-Si sample containing a buried a-Si layer and a thin buried liquid Si layer (thickness 10 nm), as a function of liquid layer depth. The initial reflectivity before irradiation is indicated (R_{ini}). A schematic drawing of the layer structure of the Cu-implanted sample is shown on top of the figure.

shown earlier,[8–11] such behavior is strongly indicative of a planar solid-liquid interface moving into the interior of the sample; the measured intensity results from interference of light reflected from the sample surface and from a moving buried interface. The following melting and solidification scenario is suggested for low-energy irradiation. During the laser pulse, melting is initiated in the buried a-Si layer due to the lower melting temperature (T_m) of a-Si [$T_{ma} \approx 1460$ K] (Ref. 5) relative to that of c-Si ($T_{mc} = 1685$ K) and as a result of the higher optical absorption coefficient of a-Si.[4] Immediately following the formation of this highly undercooled (temperature $\approx T_{ma} < T_{mc}$) liquid layer, it will start to crystallize at the interface with the c-Si surface layer. The amorphous-to-liquid-to-crystal transition is exothermic due to the difference in latent heat of melting for c-Si and a-Si.[31] Part of the heat released upon solidification is used to melt deeper lying a-Si. This deeper, undercooled liquid layer will crystallize, again releasing latent heat, and hence a continuous self-sustained ("explosive") melting and crystallization process occurs in the buried a-Si layer.

The time-resolved reflectivity measurements can be analyzed quantitatively using calculations of the reflectivity of a sample containing a thin buried liquid (l-Si) layer. The optical modeling takes into account multiple reflection from all phase boundaries. In the calculations the refractive index of the crystalline surface layer was taken at the melting temperature of a-Si.[32] Figure 4 shows the calculated reflectivity as a function of depth of a 10-nm-thick liquid layer. It can be seen that the reflectivity will decrease with respect to the initial value as soon as a buried liquid layer forms at 130-nm depth (= the position of the c-Si/a-Si interface). This is a result of destructive interference between light reflected from the surface and from the buried c-Si/l-Si interface and is clearly observed in the reflectivity transients in Fig. 3. Following this initial decrease, subsequent interference maxima and minima are expected for every 52 nm ($= \frac{1}{4}\lambda$ in the sample) propagated by the buried liquid layer. These interference oscillations are observed in the reflectivity transients for 0.14–0.23 J/cm^2. The number of interference extrema is determined by the maximum propagation depth of the EC process. For 0.20-J/cm^2 irradiation, seven extrema are observed, apart from the initial decrease. The calculations of Fig. 4 indicate that in this case the buried liquid layer has fully consumed the a-Si layer. For lower-energy densities fewer extrema are observed, indicating that the EC process was quenched within the a-Si layer. Quenching can occur when the heat released by crystallization is balanced by heat flow into the well-conducting c-Si substrate. The EC velocity can be calculated by dividing $\frac{1}{4}\lambda$ by the measured time delay between subsequent interference extrema. For 0.20 J/cm^2 irradiation, this yields a velocity of 16.2 ± 1.2 m/s, constant over the depth within the error.[33]

For irradiation at 0.23 J/cm^2, an increase in reflectivity superimposed on the last few extrema is observed. For higher-energy densities this effect becomes more pronounced; in the reflectivity transients for 0.28 and 0.49 J/cm^2, a high-reflectivity plateau is observed after the initial decrease in reflectivity. The absolute value of this plateau ($R = 75\%$) corresponds to that of an optically thick liquid layer at the surface. This layer shields the buried l-Si layer from the probe laser light, and hence no further oscillations in reflectivity are observed. This indicates that at high-energy irradiation, after initiation of melting in the buried a-Si layer, the laser pulse still supplies sufficient energy to raise the surface temperature above the melting point (T_{mc}).

2. Channeling

Figure 5 shows RBS spectra for samples irradiated at energy densities ranging from 0.20 to 0.67 J/cm^2, analyzed in channeling and random direction. In addition, a channeling spectrum for the as-implanted sample is shown. The channeling spectra can be interpreted by comparing the scat-

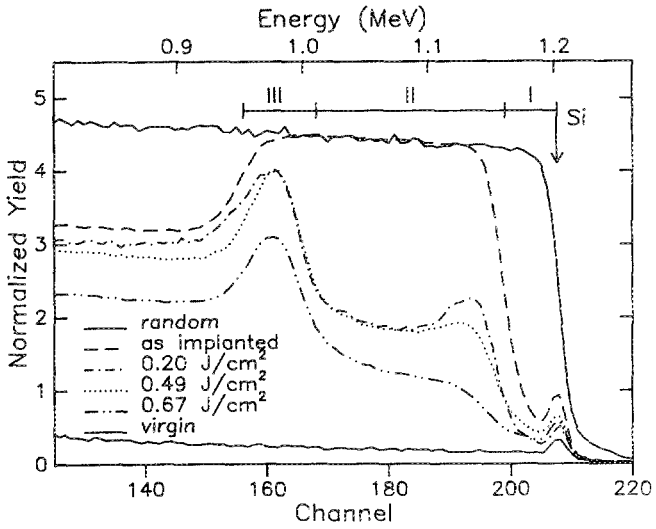

FIG. 5. Channeling spectra for Cu-implanted Si(100) samples before and after irradiation at various energy densities (indicated in the figure). A random spectrum and a channeling spectrum for a virgin sample are shown for reference.

tering yield with that from a virgin Si(100) sample, which is shown for reference. In the spectrum of the as-implanted sample, a low yield is observed near the surface backscattering energy (region I indicated in the figure), indicating the presence of a crystalline surface layer, in agreement with the TEM observation (Fig. 1). Between channel 160 and 190, the channeling yield equals the random scattering height (regions II and III). This indicates that a fully disordered region has formed. The thickness of this region estimated from the channeling spectrum is 485 nm. This is equivalent to the combined thickness of the buried *a*-Si layer and the most heavily damaged part of the *c*-Si substrate as observed in TEM. After irradiation at energy densities between 0.20 and 0.49 J/cm^2, the yield from the originally amorphous layer (region II) decreases to $\approx$40% of the random height. This implies that the amorphous layer has crystallized with a large degree of order in the [100] direction. The remaining peak in region III corresponds to the EOR damage as observed in the TEM micrograph of Fig. 1.

3. Cu redistribution

Figure 6(a) shows the Cu concentration as a function of depth before and after irradiation at 0.23 J/cm^2. Data are derived from RBS spectra. It can be seen that after irradiation Cu has been transported deeper into the sample. This is further evidence that a buried liquid layer has moved through the sample: Cu exhibits strong segregation effects at the *l*-Si/*c*-Si interface and thus is zone-refined inward, with the self-propagating liquid layer.[6] After irradiation, the Cu concentration peaks at $\approx$500-nm depth. This indicates that Cu is zone refined over the full thickness of the originally *a*-Si layer and is trapped near the interface with the *c*-Si substrate. The Cu concentration profile after irradiation at 0.67 J/cm^2 is shown in Fig. 6(b). Again, an inward segregation of Cu can be seen. In addition, a Cu peak is observed at the surface. This will be discussed later on.

4. Cross-section TEM

To study the microstructure in more detail, a sample irradiated at 0.35 J/cm^2 was investigated by TEM. Figure 7(a) shows a (011) cross-section TEM micrograph in which three distinct regions on top of the *c*-Si substrate can be observed.

(I) A 130-nm-thick crystalline surface layer. The top 100 nm of this layer contains a low density of dislocations.

(II) The originally amorphous region, which was explosively crystallized (thickness 370 nm). Selected-area electron diffraction [Fig. 7(b)] reveals that this region is single crystalline with the same orientation as the surface region. Besides the bright spots of the Si matrix, small spots corresponding to twinned regions are observed. Such regions can be seen in the bright-field image of Fig. 7(a) and are marked "T." Twins are oriented parallel to {111} planes, inclined at 35° to the surface normal. In Fig. 7(a) also "boundaries" parallel to [100] can be observed (marked "→"). These boundaries separate [100] oriented columns with a lateral dimension of 50–200 nm. A highly defected region is observed near the interface with region I.

(III) A defected region (thickness $\approx$160 nm) beneath the crystallized layer. The dark contrast in the micrograph is characteristic of EOR damage. This region corresponds to

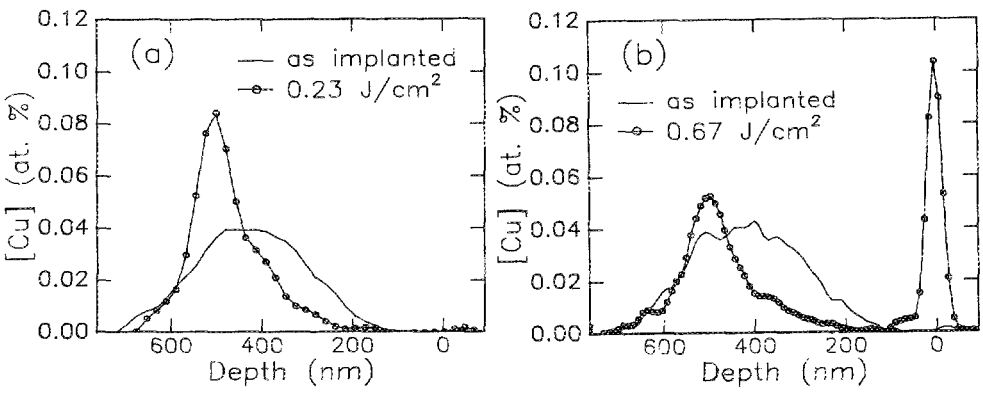

FIG. 6. Cu concentration as a function of depth after implantation and after irradiation at (a) 0.23 J/cm^2 and (b) 0.67 J/cm^2. Concentration profiles are derived from RBS spectra.

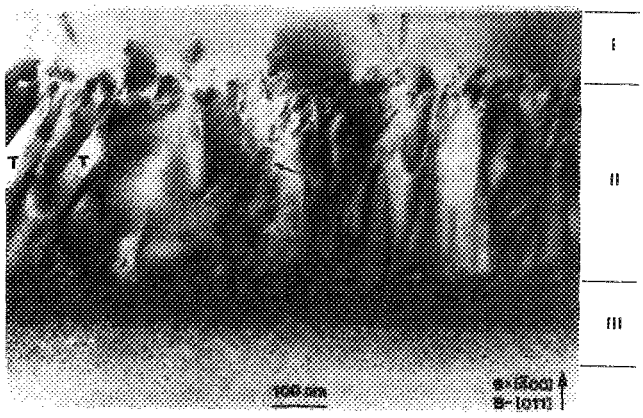

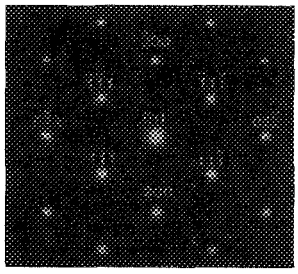

FIG. 7. (011) Cross-section TEM micrographs of a Cu-implanted Si(100) sample after pulsed-laser irradiation at 0.35 J/cm^2. (a) [400] bright-field image. Twins are marked "T" and boundaries parallel to [100] are indicated "→". (b) Electron diffraction pattern from the crystallized Si layer. Images of primary spots mirrored with respect to the axis through $[\bar{1}\bar{1}1]$ and $[11\bar{1}]$ or with respect to the axis through $[1\bar{1}1]$ and $[\bar{1}1\bar{1}]$ correspond to twinned regions. Other spots are attributed to double diffraction.

FIG. 8. High-resolution image of solidification structures shown in Fig. 7(a): interface between region I and II. Interfaces between "boundary" region and crystalline columns are indicated "→".

the high-yield portion (region III) in the channeling spectra of irradiated samples in Fig. 5.

High-resolution imaging was employed for a detailed study of the nature and origin of the specific defect structures. The imaging conditions were chosen such that the resulting image contrast was a 3.14-Å crossed fringe pattern in crystal matrix regions. Figure 8 shows a high-resolution micrograph of the interface region between I and II. The top of this figure shows part of the crystalline Si surface layer (region I). Furthermore, fringe patterns are clearly observed on the left and right bottom side of the micrograph, corresponding to [100]-crystalline ordering in the explosively crystallized columns. No such fringes are visible in the "boundary" region in the middle of the bottom region of the micrograph (interfaces between columns and boundary are indicated "→"). This indicates that boundary regions are composed of misoriented crystalline or even amorphous material. Boundary regions are typically 10–20 nm wide and extend deep into region II. No amorphous or microcrystalline areas are detected in the [100]-oriented columns.

Figure 9 shows another image of the interface region between I and II. The top of this figure shows part of the crystalline Si surface layer. The base of the figure shows crystalline Si formed by the epitaxial explosive crystallization process. In addition, the figure shows part of a boundary. A large number of microtwins (marked "t") are observed in the region where EC has started. These twins are only a few interplanar distances (d_{111}) thick. Furthermore, a large twin lamella (marked "T") is observed, with intensity modulations with a period $3d_{111}$. Such fringes are characteristic for the overlap of a twin with perfectly oriented matrix material. This large twin lamella is similar to the long and broad lamellae in Fig. 7(a). The detailed image in Fig. 9 shows that these large twins originate at the boundaries parallel to [100].

FIG. 9. High-resolution image of solidification structures shown in Fig. 7(a): interface between region I and II. Twins are indicated "t" and "T".

5. Discussion

The time-resolved measurements, combined with the detailed microstructural investigations, strongly suggest the following transient melting and solidification scheme. During irradiation, a liquid layer is formed in the buried a-Si, at the interface with the c-Si surface layer. This molten layer immediately starts to solidify epitaxially, seeded from the c-Si surface region. Heat released upon solidification can be used to melt deeper lying a-Si and hence explosive epitaxial crystallization occurs. The interface region where crystallization starts is not atomically sharp, as is shown by the TEM micrograph obtained from a sample after implantation (Fig. 1). Hence it is very likely that inhomogeneous nucleation occurs at the c-Si/a-Si interface. Possibly, transient stress effects, related to the difference in density between liquid and solid Si, can also play a role in this respect. Inhomogeneous nucleation can give rise to dense microtwin formation on {111} planes in the initial stage of crystallization. There are four sets of {111} planes on which twinning can occur. During growth, these twins intersect and growth of most twins is impeded after a growth distance of ≈ 30 nm. Only a few twins extend deep into the crystal. Furthermore, due to the inhomogeneous nucleation, growth cannot occur in a layer-by-layer fashion, via subsequent (100) plane nucleation.[3] Instead, isolated growth events are initiated in the interface region and growth proceeds via [100]-oriented columns. Possibly the size of columns is related to the distance between nucleation sites. The columns are separated by a zone of misoriented or amorphous Si. These boundary zones provide nucleation sites for formation of twin lamellae. Most of these twins protrude deep in the crystallized layer.

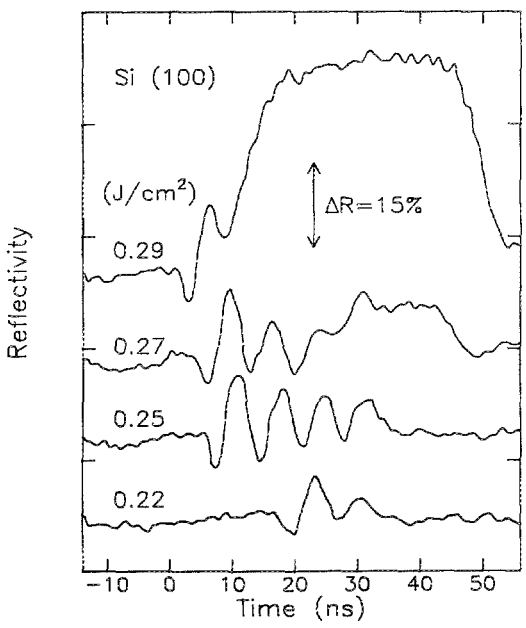

FIG. 10. Transient reflectivity measurements recorded during pulsed-laser irradiation of Si-implanted Si(100) samples at different laser energy densities (indicated in the figure). Subsequent reflectivity transients are each shifted by an absolute scale of 15% for clarity, and the arrow indicates the reflectivity scale. The steady-state reflectivity before irradiation amounts to 35% for all transients. The peak of the laser pulse is taken as the origin of the time axis.

TEM was used to characterize the microstructure obtained after 0.35-J/cm^2 irradiation only. The channeling spectra in Fig. 5 indicate the evolution of the microstructure over a larger energy-density range. It can be seen that for energy densities between 0.20 and 0.49 J/cm^2, the defect formation process is not strongly dependent on energy density; in all cases the backscattering yield from region II reaches a level of $\approx 40\%$. Therefore, the TEM micrograph taken after 0.35-J/cm^2 irradiation can be taken as representative for all phenomena in this energy-density range. The channeling yield of 40% is attributed to dechanneling and direct scattering from twinned regions, boundaries, and misaligned areas.

A more complicated scenario is derived for irradiation at 0.67 J/cm^2. TRR measurements show that in this case surface melting is induced after initiation of EC of the buried amorphous layer. At high-energy density this surface melt can probably penetrate beyond the interface between regions I and II, thereby remelting microtwins, originally formed during EC several nanoseconds earlier. After reaching the maximum melt penetration depth, the surface melt starts to solidify, seeded from the epitaxially crystallized buried layer. This scenario explains the further reduction in channeling yield from region II, as is observed in Fig. 5. The surface-melt zone refines part of the Cu toward the surface, and causes the Cu pileup at the surface as observed in Fig. 6(b).

B. Si implanted samples: Si(100) vs Si(111)

1. Si(100)

Figure 10 shows a compilation of TRR transients obtained during pulsed-laser irradiation of the Si-implanted and thermally annealed Si(100) samples as described in Sec. III B. Analogous to the TRR measurement for the Cu-implanted samples, oscillations in the reflectivity are observed for low-energy irradiation. The threshold energy-density for melting in the a-Si is 0.22 J/cm^2. For energy densities of 0.29 J/cm^2 and higher, oscillations are followed by a high-reflectivity plateau corresponding to the reflectivity of an optically thick l-Si layer at the surface. For all transients, initially a decrease in reflectivity is observed, which is in agreement with the formation of a liquid layer at 130-nm depth, at the c-Si/a-Si interface. Indeed, these measurements suggest that also in the Si-implanted samples the buried a-Si layer is transformed to c-Si via explosive crystallization.

A detailed investigation of the microstructure after irradiation was performed using cross-section TEM. A (011) cross-section micrograph of a sample irradiated at an energy density of 0.35 J/cm^2 is shown in Fig. 11(a). Four distinct regions on top of the c-Si substrate can be observed.

(I) A 130-nm-thick crystalline surface layer. The top 100 nm of this layer contains a low density of dislocations.

(II) The explosively crystallized layer with a thickness varying between 350 and 420 nm. This region is single crystalline with two lamellae protruding deep into the crystallized layer. Also, the characteristic boundaries parallel to [100] are observed. Along these boundaries, near the inter-

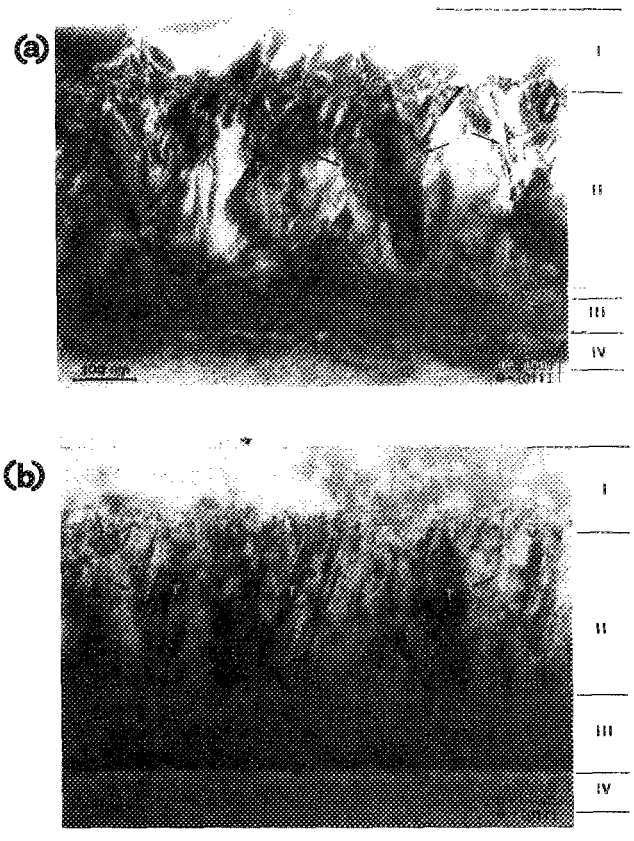

FIG. 11. (011) Cross-section [$\bar{4}00$] bright-field TEM micrograph of a Si-implanted and thermally annealed Si(100) sample after pulsed-laser irradiation at 0.35 J/cm^2. Twins are marked "T", and boundaries parallel to [100] are indicated "→". (a) Si(100) and (b) Si(111).

face with region III, large pockets of microtwins are observed. High-resolution imaging did not show amorphous or microcrystalline areas in the crystalline columns in region II. The interface with region I is heavily defected. High-resolution microscopy reveals that this area contains a large density of microtwins, similar to those described for the Cu-implanted sample in Sec. IV A 4.

(III) A remaining amorphous region, with a thickness varying between 0 and 70 nm. The presence of this layer indicates that EC was quenched before reaching the *c*-Si substrate.

(IV) A defected crystalline region (thickness $\approx$60 nm), containing EOR damage.

The time-resolved measurements, combined with the detailed microstructural analyses, suggest a transient melting and solidification scheme similar to that observed for Cu-implanted samples, as described in Sec. IV A 5: Buried amorphous layers produced by Si implantation can be converted to single-crystalline Si via epitaxial explosive crystallization. In the initial stage, solidification does not proceed via (100) layer-by-layer growth, probably due to interface roughness (see Fig. 2), resulting in inhomogeneous nucleation. This may lead to formation of columnar structures of epitaxially grown *c*-Si.

2. Si(111)

Si(111) samples were implanted, thermally annealed, and pulsed-laser irradiated similarly to the Si(100) samples. The TRR measurements (not shown) show qualitatively the same behavior: During low-energy-density irradiation, oscillations are observed, indicating the occurrence of EC. For higher-energy densities a high-reflectivity plateau is observed, indicating surface melting.

Figure 11(b) shows a (011) cross-section TEM micrograph for a Si(111) sample irradiated at 0.35 J/cm^2. Four distinct regions can be observed in the figure.

(I) A 120-nm-thick crystalline surface layer containing dislocation loops. Similar loops are observed in the sample before irradiation (Fig. 2).

(II) A $\approx$280-nm-thick crystalline layer. This layer contains both [111] oriented columns and a high density of twins, extending from the crystalline surface region towards a remaining amorphous region. Twins are oriented parallel to {111} planes, inclined at 19.5° to the surface normal. The micrograph also shows the characteristic boundaries (indicated "→"), separating [111]-oriented columns. Near the interface with region III, large pockets of microtwins are observed along these boundaries. High-resolution microscopy also shows a large density of microtwins near the interface with region I. Microtwins parallel to the (111) growth plane were also observed.

(III) A remaining amorphous region, with a thickness varying between 130 and 150 nm.

(IV) A defected crystalline region containing EOR damage.

3. Comparison between experiments on Si(100) and Si(111)

As discussed in the preceding paragraphs, in both Si(100) and Si(111) EC of buried amorphous Si layers yields single-crystalline Si aligned with the surface, with large twins extending into the layer. Twinning is more pronounced in Si(111) samples. An important parameter in the analysis of these features is the crystallization velocity. Figure 12 shows this velocity as a function of depth in both Si(100) and Si(111) samples. Velocities are obtained from TRR measurements during 0.25-J/cm^2 irradiation (shown as an inset in the figure) combined with optical calculations of the reflectivity as in Fig. 4. It can be seen that the interface velocity is constant over the depth, at an average of 15.6 m/s for Si(100) and 14.6 m/s for Si(111), respectively. Results of a series of equivalent measurements on similar samples were averaged to reduce statistical variations, resulting in a relative error[34] of $\pm$ 0.3 m/s for the two measured crystallization velocities. It should be noted that rapid epitaxial crystallization phenomena, at similar velocities as described here, have also been found by Cullis, Webber, and Chew.[35] However, the present data are the first to show self-sustained crystallization at this high rate.

Several workers[36–38] have studied the orientation dependence of high-speed crystal growth from the melt. It has been shown that 15 $\pm$ 1.5 m/s is a critical limit for epitaxial regrowth of Si(100).[36] If the quench rate is enhanced above this velocity, crystal growth breaks up and amorphous material forms. In the present experiments, explosive epitaxial crystal growth in Si(100) occurs just at this threshold velocity. Cullis *et al.*[37] have shown that just below the threshold,

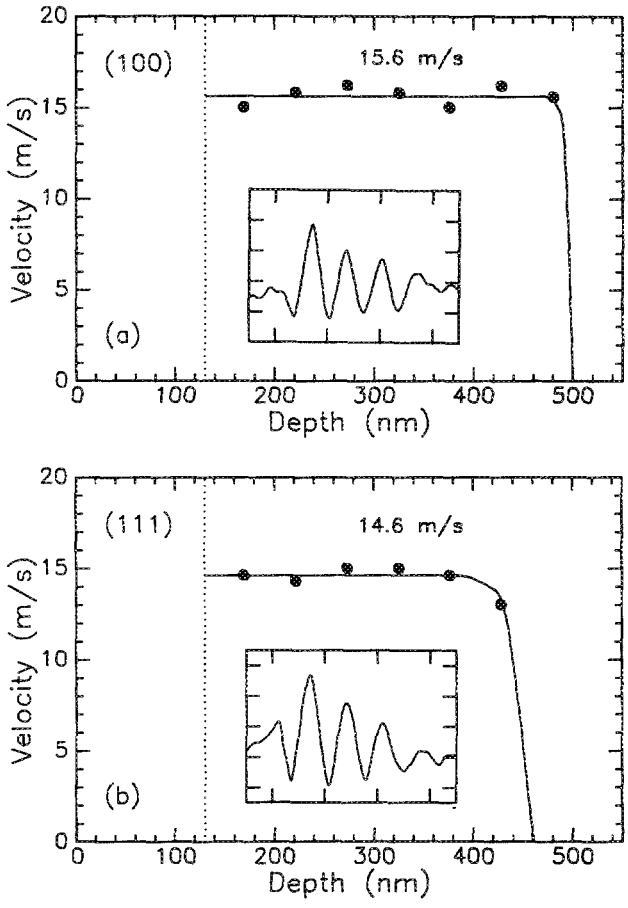

FIG. 12. Solid-liquid interface velocity for explosive crystallization in Si-implanted samples during irradiation at 0.25 J/cm^2. The closed circles are measured data obtained from TRR transients shown as an inset in the figure. The drawn lines are averages from an extended series of experiments. The dotted line indicates the c-Si/a-Si interface. (a) Si(100) and (b) Si(111).

Si(100) would grow almost perfectly, without twin or column formation. The present experiments, however, do not exhibit this perfect solidification scheme. As discussed before, this can be understood from the fact that crystallization starts from a rough transition region.

Plane nucleation on the densely packed Si(111) planes is kinetically less favored than on Si(100). Hence the maximum velocity for epitaxial growth of Si(111) is expected to be lower than that of Si(100). Cullis *et al.*[37] have estimated this velocity to be 5–8 m/s. For higher velocities they have observed a different growth mode, with dense twinning and defect formation. This enhanced crystal growth mode has been explained by the presence of nucleation sites at grooves in the growing surfaces.[39,40] The amorphization threshold for this mode was determined to be ≈ 12 m/s.[37] The present experiments, however, show that Si(111) crystal growth can still take place at 14.6 m/s. It should be noted that the 12-m/s limit is a first-order estimate based on a heat-flow calculation which did not take into account undercooling effects. In addition, as nucleation at twin boundaries plays a role, the maximum velocity must be related to the twin density, which can easily change from one experiment to the other.

TEM shows that for the same irradiation fluence of 0.35 J/cm^2, the quench depth for growth in Si(100) is larger than that for growth in Si(111) (i.e., 515 ± 35 nm vs 400 ± 10 nm). A similar effect is observed in the TRR transients of Fig. 12. This can be understood from the difference in solidification velocity for the two crystal orientations. During the slower solidification in Si(111), more heat diffuses away into the substrate, reducing the amount of heat available for melt penetration. In addition, growth breakdown could occur earlier in the Si(111) sample due to the dense twin formation.

C. Ar-implanted samples

Ar-implanted SOS samples were irradiated with a ruby laser pulse. Figure 13 shows the combined transient reflectivity and conductivity measurements obtained during 0.25-J/cm^2 irradiation. The reflectivity measurements show extrema, numbered 1, 2, and 3 in the figure. Usually, optical measurements on the multilayer structure of SOS samples are complicated by the occurrence of interference effects during heating of the sample.[41] Upon heating, the refractive index of Si and sapphire increase; hence the interference condition and the sample reflectivity will change. The initial decrease in reflectivity between $t = 0$ and $t = 10$ ns can be attributed to this effect.[11] The rapid variations later in time are indicative of the formation and propagation of a buried liquid layer in the sample, as discussed in detail in the previous sections. Optical calculations as in Fig. 4 reveal that for an EC process completely converting the relatively thin (150 nm) buried amorphous layer, three interference extrema (one maximum and two minima) are expected. This is as observed in Fig. 13. Channeling data (not shown) revealed that EC has converted the a-Si layer to c-Si with a large degree of ordering epitaxial to the c-Si surface layer.

The thickness of the buried liquid layer can be directly determined from the time-resolved conductivity measurement performed simultaneously. Figure 13 shows that the effective melt thickness reaches a maximum of 16 nm. The timing of the interference extrema indicates that at that time the EC process has converted half of the a-Si layer to c-Si. Eventually, the buried liquid layer thickness decreases, and

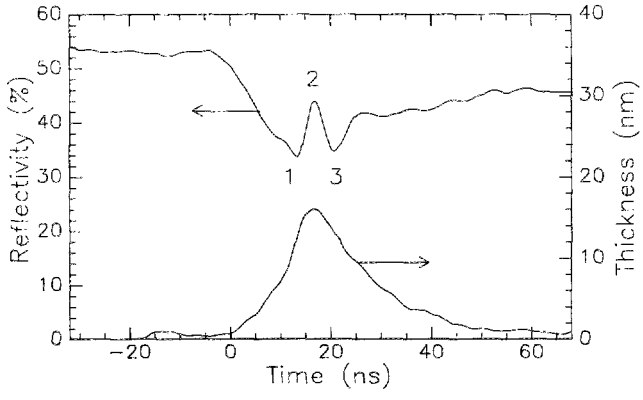

FIG. 13. Combined time-resolved reflectivity and conductivity measurements recorded during pulsed-laser irradiation of Ar-implanted SOS samples at 0.25 J/cm^2. The conductivity transient was converted to melt thickness. The timing is taken relative to the peak of the laser pulse.

at $t = 40$ ns no significant signal is observed anymore. At the same time also the reflectivity level reaches a steady level, only slightly increasing as a result of cooling of the SOS layer structure.

D. 600-keV Si-implanted samples

Pulsed-laser irradiation has also been applied on thicker and deeper buried a-Si layers, as produced by 600-keV Si implantation (see Table I). From channeling measurements it is concluded that in this case EC has proceeded with ordering in the [100] direction as well.

V. COMPARISON BETWEEN IMPLANTATIONS

Table II shows the measured EC velocity for all samples studied. The characteristic features derived from the full range of experiments can be summarized as follows.

(1) The TRR measurements for Cu-implanted samples (Fig. 3) and those for Si-implanted samples (Fig. 10) show a quantitatively different behavior, although the sample geometry is nearly equal for the two cases. While the threshold energy density for surface melting is the same for the two types of samples (≈ 0.28 J/cm^2), the threshold for melting in the a-Si is quite different: 0.14 J/cm^2 for Cu-implanted samples and 0.22 J/cm^2 for Si-implanted samples. One suggestion is that this difference originates from the presence of the Cu impurity, which could reduce the local melting temperature. However, the Cu concentration at the c-Si/a-Si interface as measured in Fig. 6 is less than 50 ppm, which we think is too low to account for any measurable effect. The difference in melt threshold can possibly be explained by the fact that the Si-implanted samples are thermally annealed after implantation, while the Cu-implanted samples are not. It is known that thermal annealing induces structural relaxation in a-Si.[42,43] As a consequence, thermal and optical properties will change in the direction of values for c-Si.[44,45] This causes the threshold energy density for buried melting to increase.

(2) Channeling implantation results in a well-defined layer structure with relatively sharp interfaces. In these samples epitaxial crystallization of the buried a-Si layer can be induced, without applying thermal annealing before irradiation. Samples which are implanted in a random direction can be crystallized epitaxially if an annealing treatment (490 °C for 15 min) is applied before irradiation. This treatment sharpens up the transition region between c-Si and a-Si. In additional experiments, not reported here, a more extensive thermal treatment has been used with the aim to produce a c-Si/a-Si interface as sharp as possible. This was done using SPE at 540 °C for 15 min. It was found that also in this case EC yielded defected single-crystalline Si, with a minimum channeling yield of 40%.

(3) In all experiments the velocity of epitaxial explosive crystallization lies in the range 15–16 m/s and is constant over the depth. The presence of Cu or Ar impurities at concentrations in the ranges 0.01–0.1 at. % does not influence this velocity to a measurable extent.

TABLE II. Epitaxial explosive crystallization velocity for the samples studied in this work.

Target	Ion	EC velocity[a] (m/s)
Si(100)	Cu^+	16.2 ± 0.9
Si(100)	Si^+	$15.6 \pm 0.6(0.3)$[b]
Si(111)	Si^+	$14.6 \pm 0.6(0.3)$[b]
(100)SOS	Ar^+	14.7 ± 0.9

[a] The systematic error due to the uncertainty in refractive index (5%) is not included (Refs. 33 and 34).

[b] The error including the timing inaccuracy is 0.6 m/s. In the comparison between velocities for (100)- and (111)-oriented samples, the error is 0.3 m/s.

VI. COMPUTER MODELING OF PHASE TRANSFORMATIONS

A. Heat-flow model

To model the phase transformations during irradiation, computer simulation was employed, using a one-dimensional heat-flow code developed by Wood and Geist.[21] In this code, the sample is represented by an array of cells of specific structure (a-Si, c-Si, l-Si), and the thermal interaction between cells is determined by thermal properties as described elsewhere.[4] Numerically calculated results converged for a cell thickness of 3 nm. This thickness was used in the simulations described hereafter. The melting temperature of a-Si was taken to be 225 K below that of c-Si.[5] Simulations were performed under the constraint that a l-Si cell, undercooled with respect to T_{mc} and in contact with a c-Si cell, would crystallize at a velocity equal to the measured 15.6 m/s for Si(100). The layer structure was chosen equal to that of the 350-keV Si-implanted Si samples after annealing, as described in Sec. III B.

B. Results

Taking appropriate energy density of the laser pulse, the simulations showed that melting was initiated at the buried c-Si/a-Si interface. It is found that the molten layer solidifies from the c-Si surface seed, and the heat of crystallization which is released is sufficient to melt deeper lying a-Si. Figure 14 summarizes the calculated phase transformation sequence in a depth-phase-time diagram. This diagram, the concept of which was introduced by Wood and Geist,[21] shows the time evolution of the boundaries between the various phases. The figure shows the initial formation of a buried molten layer and subsequent explosive propagation of the liquid layer converting a-Si to c-Si. The thickness of the liquid layer initially increases as a function of time, reaching a maximum of 40 nm. As the melt proceeds further inwards, the heat flow is influenced by the different thermal properties of the c-Si substrate. This causes the melt thickness to decrease and eventually results in quenching at a depth of 480 nm. This simulation clearly shows that the ex-

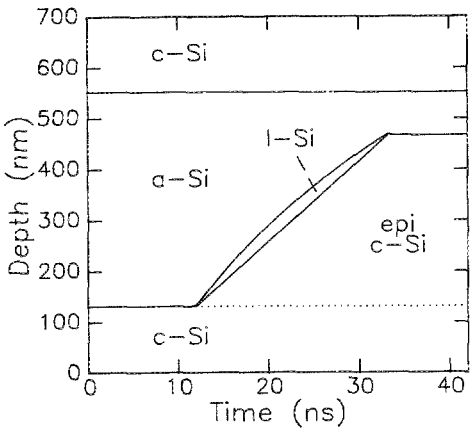

FIG. 14. Depth-phase-time diagram for epitaxial explosive crystallization obtained using computer simulation of transient heat flow and phase transformations. The peak of the laser pulse is taken as the origin of the time axis.

plosively propagating phase transformations can be analyzed in terms of standard heat flow.

The simulated data are in qualitative agreement with the experimental results. Indeed, quenching is observed in the experiments, for a specific energy density. Also, the gradual increase in thickness of the buried melt, followed by a decrease, has been directly observed in the transient conductivity measurements of Fig. 13. The difference in maximum melt thickness between experiment and simulation (i.e., 40 nm vs 16 nm) is due to the specific choice of layer geometry in the latter. Additional simulations (not shown) for the layer geometry of the implanted SOS samples yield a maximum melt thickness of 16 nm, in perfect agreement with the measured data. In thin buried *a*-Si layers, the maximum melt thickness is reduced as a result of heat flow into the well-conducting *c*-Si substrate.

VII. NUCLEATION OF EXPLOSIVE CRYSTALLIZATION

As noted in Sec. IV, no microcrystalline grains were observed in the solidification structures formed by epitaxial explosive crystallization of buried *a*-Si layers. This indicates that the nucleation and growth processes which sustain explosive crystallization of amorphous surface layers, and which yield randomly oriented polycrystalline Si (*pc*-Si), do not play a role under the present experimental conditions. Such processes may involve heterogeneous nucleation at the leading *a*-Si/*l*-Si interface, as suggested by Tsao and Peercy,[14] and solid-state nucleation in *a*-Si during the heating period prior to melting, as recently suggested by Roorda and Sinke.[15] The difference in solidification behavior can be interpreted as follows.[46]

(1) The nucleation processes yielding *pc*-Si must compete with *c*-Si growth which starts immediately at the *c*-Si surface seed, as soon as a buried liquid layer is formed. In additional experiments, which will be reported elsewhere,[47] it is shown that the *pc*-Si nucleation and growth processes exhibit a characteristic time delay for triggering of EC of > 10 ns. Consequently, these processes cannot trigger EC in buried *a*-Si layers.

(2) During EC in buried *a*-Si layers, a planar heat source is available at the freezing *c*-Si/*l*-Si interface, and the liquid temperature can locally increase well above T_{ma}.[48] Small *pc*-Si nuclei have a melting point well below that of bulk *c*-Si,[49,50] and hence, if they are formed, they can probably be remelted. As a consequence, epitaxial growth can proceed without being impeded by *pc*-Si nuclei present in the liquid. In EC of *a*-Si surface layers, such a planar heat source is not available and a more homogeneous temperature distribution builds up. Under these conditions *pc*-Si are not remelted and EC is sustained by growth of these nuclei, yielding randomly oriented *pc*-Si. Preliminary heat-flow calculations support this suggestion.

VIII. CONCLUSIONS

Ion implantation in the energy range from 275 to 600 keV can be used to form amorphous silicon layers buried in a crystalline matrix. Pulsed-laser irradiation can be employed for crystallization of the buried amorphous layers. Under specific irradiation conditions internal melting occurs at the *a*-Si/*c*-Si interface, immediately followed by explosive crystallization (EC) of the buried layer. EC is mediated by a buried liquid layer of typically 10–40 nm in thickness, and proceeds epitaxially in both Si(100) and Si(111) samples, with formation of twins. Twin formation is most pronounced in Si(111). Crystal growth velocities range from 15 to 16 m/s, close to the fundamental limit for crystalline ordering at a Si liquid-crystalline interface. Nucleation of polycrystalline Si, which sustains EC of *a*-Si surface layers, is suppressed in experiments concerning buried *a*-Si layers.

ACKNOWLEDGMENTS

M. O. Thompson (Cornell University) is gratefully acknowledged for providing patterned SOS samples for transient conductivity measurements. We also acknowledge R. F. Wood and G. A. Geist (Oak Ridge National Laboratory) for making the heat-flow code available, A. G. Cullis (RSRE, Malvern) for fruitful discussions, and J. J. P. Bruines and M. P. A. Viegers (Philips Research Laboratories) for critically reading the manuscript. Eventually, we would like to thank F. W. Saris, S. Roorda, and A. M. Vredenberg for their stimulating interest throughout the course of this work. The work at the FOM-Institute is part of the research program of the Stichting voor Fundamenteel Onderzoek der Materie (FOM) and was made possible by financial support from the Stichting voor Technische Wetenschappen (STW) and the Nederlandse Organisatie voor Wetenschappelijk Onderzoek (NWO)

[1] See, for instance, *Ion Implantation: Science and Technology*, 2nd ed., edited by J. F. Ziegler (Academic, Boston, 1988).

[2] For a recent overview, see Proceedings of the 7th International Conference on Ion Implantation Technology, edited by T. Takagi, Nucl. Instrum. Methods B **37/38** (1989); Proceedings of the 6th International Conference on Ion Beam Modification of Materials, edited by S. Namba, N. Itoh, and M. Iwaki, Nucl. Instrum. Methods B **39** (1989).

[3] J. M. Poate and J. W. Mayer, Eds., *Laser Annealing of Semiconductors*

(Academic, New York, 1982).
[4]R. F. Wood and G. E. Jellison, in *Semiconductors and Semimetals*, edited by R. F. Wood, C. W. White, and R. T. Young (Academic, New York, 1984), Vol. 23.
[5]M. O. Thompson, G. J. Galvin, J. W. Mayer, P. S. Peercy, J. M. Poate, D. C. Jacobson, A. G. Cullis, and N. G. Chew, Phys. Rev. Lett. **52**, 2360 (1984).
[6]W. Sinke and F. W. Saris, Phys. Rev. Lett. **53**, 2121 (1984).
[7]J. Narayan, S. J. Pennycook, D. Fathy, and O. W. Holland, J. Vac. Sci. Technol. A **2**, 1495 (1984).
[8]D. H. Lowndes, G. E. Jellison, S. J. Pennycook, S. P. Withrow, and D. N. Mashburn, Appl. Phys. Lett. **48**, 1389 (1986).
[9]J. J. P. Bruines, R. P. M. van Hal, H. M. J. Boots, A. Polman, and F. W. Saris, Appl. Phys. Lett. **49**, 1160 (1986).
[10]D. H. Lowndes, S. J. Pennycook, G. E. Jellison, S. P. Withrow, and D. N. Mashburn, J. Mater. Res. **2**, 648 (1987).
[11]K. Murakami, O. Eryu, K. Takita, and K. Masuda, Phys. Rev. Lett. **59**, 2203 (1987).
[12]P. S. Peercy, J. Y. Tsao, S. R. Stiffler, and M. O. Thompson, Appl. Phys. Lett. **52**, 203 (1988).
[13]W. C. Sinke, T. Warabisako, M. Miyao, and T. Tokuyama, Appl. Surf. Sci. **36**, 460 (1989).
[14]J. Y. Tsao and P. S. Peercy, Phys. Rev. Lett. **58**, 2782 (1987).
[15]S. Roorda and W. C. Sinke, Appl. Surf. Sci. **36**, 188 (1989).
[16]J. J. P. Bruines, thesis, Eindhoven Technical University (1988).
[17]Primary results have been submitted by A. Polman, D. J. W. Mous, P. A. Stolk, W. C. Sinke, C. W. T. Bulle-Lieuwma, and D. E. W. Vandenhoudt, Appl. Phys. Lett. **55**, 1097 (1989).
[18]D. H. Auston, C. M. Surko, T. N. C. Venkatesan, R. E. Slusher, and J. A. Golovchenko, Appl. Phys. Lett. **33**, 437 (1978).
[19]R. M. A. Azzam and N. M. Bashara, *Ellipsometry and Polarized Light* (North-Holland, Amsterdam, 1987).
[20]G. J. Galvin, M. O. Thompson, J. W. Mayer, R. B. Hammond, N. Paulter, and P. S. Peercy, Phys. Rev. Lett. **48**, 33 (1982).
[21]R. F. Wood and G. A. Geist, Phys. Rev. B **34**, 2606 (1986); G. A. Geist and R. F. Wood, Oak Ridge National Laboratory No. ORNL-6242, 1985 (unpublished).
[22]W. K. Chu, J. W. Mayer, and M. A. Nicolet, *Backscattering Spectrometry* (Academic, New York, 1978).
[23]L. R. Doolittle, Nucl. Instrum. Methods B **9**, 344 (1985).
[24]C. W. T. Bulle-Lieuwma and P. C. Zalm, Surf. Interface Anal. **10**, 210 (1987).
[25]R. G. Wilson, J. Appl. Phys. **60**, 2797 (1986).
[26]J. F. Ziegler, J. P. Biersack, and U. Littmark, *The Stopping and Range of Ions in Solids* (Pergamon, New York, 1984), Vol. 1.
[27]O. W. Holland, M. K. El-Ghor, and C. W. White, Appl. Phys. Lett. **53**, 1282 (1989).
[28]J. Narayan, D. Fathy, O. S. Oen, and O. W. Holland, Mater. Lett. **2**, 211 (1984).
[29]G. L. Olson and J. A. Roth, Mater. Sci. Rep. **3**, 1 (1988).
[30]P. A. Stolk, A. Polman, W. C. Sinke, C. W. T. Bulle-Lieuwma, and D. E. W. Vandenhoudt, Mater. Res. Soc. Conf. Proc. **147**, (1989) (to be published).
[31]E. P. Donovan, F. Spaepen, D. Turnbull, J. M. Poate, and D. C. Jacobson, Appl. Phys. Lett. **42**, 698 (1983).
[32]A complex index of $4.05 - 0.045i$ was used, obtained from an extrapolation of data in the temperature range 25–500 °C by G. E. Jellison and H. H. Burke, J. Appl. Phys. **60**, 841 (1986), and data near T_{mc} by M. O. Lampert, J. M. Koebel, and P. Siffert, J. Appl. Phys. **52**, 4975 (1981).
[33]The error in the velocity is determined by the estimated uncertainty in index (5%), the system timing inaccuracy (3%), and the standard deviation in the velocity data determined as a function of depth (5% for the Cu-implanted samples).
[34]The errors are determined by the standard deviation in the average velocity data as a function of depth for a series of measurements. The errors in refractive index and timing lead to an additional systematic error (see Ref. 33).
[35]A. G. Cullis, H. C. Webber, and N. Chew, Appl. Phys. Lett. **40**, 998 (1982).
[36]M. O. Thompson, J. W. Mayer, A. G. Cullis, H. C. Webber, N. G. Chew, J. M. Poate, and D. C. Jacobson, Phys. Rev. Lett. **50**, 896 (1983).
[37]A. G. Cullis, N. G. Chew, H. C. Webber, and D. J. Smith, Cryst. Growth **86**, 624 (1984).
[38]J. A. Yater and M. O. Thompson, Phys. Rev. Lett. **63**, 2088 (1989).
[39]R. S. Wagner, Acta Metall. **8**, 57 (1960).
[40]H. F. John and J. W. Faust, in *Metallurgy of Elemental and Compound Semiconductors*, edited by R. O. Grubel (Interscience, New York, 1961), pp. 127–148.
[41]K. Murakami, Y. Tohmiya, K. Takita, and K. Masuda, Appl. Phys. Lett. **45**, 659 (1984).
[42]W. C. Sinke, S. Roorda, and F. W. Saris, J. Mater. Res. **3**, 1201 (1988).
[43]S. Roorda, S. Doorn, W. C. Sinke, P. M. L. O. Scholte, and E. van Loenen, Phys. Rev. Lett. **62**, 1880 (1989).
[44]J. E. Fredrickson, C. N. Waddell, W. G. Spitzer, and G. K. Hubler, Appl. Phys. Lett. **40**, 172 (1982).
[45]E. P. Donovan, G. K. Hubler, and C. Waddell, Nucl. Instrum. Methods B **19/20**, 590 (1987).
[46]See also W. C. Sinke, A. Polman, S. Roorda, and P. A. Stolk, Appl. Surf. Sci. **43**, 128 (1989).
[47]A. Polman, S. Roorda, P. A. Stolk, and W. C. Sinke (unpublished).
[48]A. Polman, P. A. Stolk, and W. C. Sinke (unpublished).
[49]G. S. Zhdanov, Sov. Phys. Crystallogr. **21**, 706 (1977).
[50]S. J. Peppiatt and J. R. Sambles, Proc. R. Soc. London A **345**, 387 (1975).